Laser induced fragmentation: From dissociation of neutrals to three-body breakup

by

Peyman Feizollah

B.S., University of Isfahan, Iran, 2008

M.S., University of Tehran, Iran, 2012

A THESIS

submitted in partial fulfillment of the
requirements for the degree

MASTER OF SCIENCE

Department of Physics
College of Arts and Sciences

KANSAS STATE UNIVERSITY
Manhattan, Kansas

2018

Approved by:

Major Professor
Itzik Ben-Itzhak

Copyright

© Peyman Feizollah 2018.

Abstract

Ultrafast lasers allow us to study molecular dynamics on their natural timescale. The electronic dynamics can be studied using attosecond pulses, while the vibrational and rotational dynamics can be probed using tens of femtosecond and picosecond laser pulses, respectively. This capability has led to a broad understanding of the electronic dynamics in atoms and molecules as well as vibrational and rotational dynamics of molecules, which is one of the important goals in basic science. Moreover, it is possible to control quantum mechanical processes using ultrafast intense lasers.

In this thesis, we focus on a couple of experiments. The first involves quantum control of the formation of neutral molecular fragments while the second focuses on three-body fragmentation of molecules employing the native-frames analysis method, which was recently introduced by our group [J. Rajput *et al.*, Phys. Rev. Lett. **120**, 103001 (2018)].

Experimental studies focused on the formation of excited neutral D fragments from D_2 molecules are presented. We show that by manipulating the chirp of the intense laser pulses, i.e. the "time order" of the frequency components within the pulse, the formation of these fragments is controlled. To achieve this control we implement a single-prism compressor to manipulate the chirp of the laser pulses.

Three-body fragmentation of CO_2 resulting in $C^+ + O^+ + O^+$ is also studied. We show that if the two bonds break in a two-step process, i.e. a sequential breakup, the pathways from which the two identical O^+ fragments originate can be separated using the native-frames analysis method. In contrast, the two O^+ fragments cannot be distinguished if the two C–O bonds break simultaneously.

Table of Contents

List of Figures vi

Acknowledgements vii

Dedication x

1 Introduction 1

2 Chirp dependence of the formation of excited neutral D fragments from D_2 in intense ultrafast laser pulses 3

2.1 Introduction 3

2.2 Experimental technique 4

2.2.1 Laser system 5

2.2.2 FTL laser pulses 5

2.2.3 Chirped laser pulses 6

2.2.4 Manipulating the GDD of laser pulses 8

2.2.5 Detection of excited neutral fragments 10

2.3 Results and discussion 12

2.3.1 Results 12

2.3.2 A qualitative description of the experimental observation 15

2.4 Summary 18

3 Native frames: Imaging three-body breakup involving two identical fragments . . 19

3.1 Introduction 19

3.2 Experimental technique 21

3.3 Native-frames analysis method 22

3.3.1 Classical Coulomb explosion simulation 24

3.4 Results and discussion 26

3.4.1 Distinguishing the pathways of O^+ fragments in sequential breakup . 26

3.4.2 KER_{CO} in the second step 30

3.5 Summary 31

4 Summary 32

Bibliography 33

List of Figures

2.1 Negatively- and positively-chirped laser pulses in the time domain 7

2.2 Schematic diagram of the single-prism compressor 9

2.3 The GDD as a function of the distance between the corner cube and prism . 10

2.4 Schematic diagram of the apparatus used to detect neutral D fragments . . . 11

2.5 The KER associated with D* fragments production by FTL laser pulses . . . 13

2.6 The KER associated with the D* fragments generated by a few positively chirped laser pulses. 14

2.7 The KER associated with the D* fragments generated by positively- and negatively-chirped pulses. 15

2.8 Peak fitting procedure to find the branching ratios of the two low KER peaks 15

2.9 Branching ratio as a function of the GDD of the laser pulses 16

2.10 Potential energy curves of H_2 and H_2^+ 17

3.1 Newton diagram and Dalitz plot of three-body fragmentation of CO_2 20

3.2 Schematic diagram of a COLTRIMS setup 22

3.3 Jacobi coordinates and relative momenta used to analyze the data in native frames 23

3.4 Schematic diagram of a bent CO_2^{3+} 24

3.5 Calculated final angular momentum of the intermediate CO^{2+} fragment . . . 26

3.6 Labeling the two O^+ fragments by color-coding them. 27

3.7 Experimental data in native frames 28

3.8 Reconstructed sequential CO_2^{3+} events 29

3.9 The KER_{CO} distribution of the second fragmentation step of CO_2 and OCS sequential breakup. 30

Acknowledgments

There are a lot of people who had an impact on my professional life since I was an undergraduate student, and I will be thankful to them forever. In the past few years, I had the opportunity to work under the supervision of Prof. Itzik Ben-Itzhak. During this time, I was constantly learning from him how to perform experiments in the lab, how to resolve the problems that I faced when performing different complicated experiments, how to think about the collected data and interpret it, and many more things. Apart from the scientific discussions we had, we had discussions about topics not necessarily related to science which I learned from as well. I learned a lot from you Itzik, and I really appreciate, and will never forget, all the time and effort you spent teaching me. I also want to thank you for all the chocolate you brought to our different meetings.

I am also thankful for all the help I had from Prof. Kevin Carnes. Kevin is always there when you face an issue. He knows our data collection and analysis codes the best, and he always works on making them better. I really appreciate the comments you gave me about my work. Also, many thanks for reading any document I wrote and correcting my many English mistakes. Kevin, I still think dark chocolate is better than milk chocolate.

I also worked with and learned a lot from other current and former group members, Dr. Ben Berry, Bethany Jochim, Travis Severt, Dr. Kanaka Raju Pandiri, Dr. Jyoti Rajput, Dr. Mohammad Zohrabi, and Reid Erdwien. Working in the lab with these people was a good and pleasant experience for me. Also, we talked a lot while sitting in the office about the science we were doing. These discussions helped me learn what they were doing and helped me learn what I was doing more deeply. Thank you all for patiently teaching me part of what I know about our research. After spending a few years in this group, I am very happy to have such good friends.

Our group works closely with the group of Prof. Brett Esry. We had a lot of joint meetings with them, which were always interesting. I learned a lot about this field of research in these

meetings and when I talked to Brett in his office. Thank you for all the time and effort you spent to talk to me about different aspects of our research.

Part of the research I did was in collaboration with other groups in the JRM lab. I had the chance to work with Dr. Artem Rudenko and Dr. Daniel Rolles on a few projects. We had multiple meetings with them discussing the projects we were working on which were good opportunities for me to learn more. Working with them in the lab helped me gain knowledge about different experimental challenges. Also, I would like to thank Yubaraj Malakar, Balram Kaderiya, Farzaneh Ziaee, and Kurtis Borne for helping with the experiments in the beamtimes we had together.

I was also involved in a few mainly quantum control experiments in collaboration with Prof. Eric Wells from Augustana University. Working with Eric, Bethany, and Raju on making the DAZZLER pulse shaper work and using the pulses to do experiments taught me a lot.

For the pulse shaping experiments, we used the KLS laser. Dr. Vinod Kumarappan and his group, Huynh Lam and Tomthin Nganba Wangjam, maintained the laser before our beamtimes, which helped us perform our experiments. Thank you for all of your help, and sorry if occasionally you had to work hard late at night so that we could have the laser.

I was involved in a few projects in collaboration with the group of Prof. Marcos Dantus from Michigan State University. I worked closely with Dr. Nagitha Ekanayake when he was in Kansas for a few beamtimes. I want to thank them for the interesting discussions during the beamtime and our joint group meetings.

I used the PULSAR laser system for my experiments, which is maintained by Dr. Charles Fehrenbach and Dr. Kanaka Raju. Thank you for all your efforts. Also, Dr. Charles Fehrenbach is an expert in running the ECR ion source, and he helped me learn how to operate the source, which I appreciate.

The JRM lab technical staff, Chris Aikens, Justin Millette, Scott Chainey, Vince Needham, and Al Rankin, are a big help for any JRM member. They help us design and build different apparatuses, maintain them, and resolve the problems we face in a professional way. I want to thank you for all of your hard work.

When I came to the US for graduate school, I started a long journey full of unknowns. Moving to another city in your country is hard, and yet I moved to another country, which has its own challenges. However, everything started to be in place very fast. This is because of my great friends, people who I knew from before and people who I got to know in Kansas. I deeply appreciate and value their friendship. I will always be grateful for having such great friends. Most importantly, I found what now I realize is the most important feeling among all, love. I am so happy for coming to Kansas and finding the most important person of my life thousands of miles away from home. Bethany, I cannot wait for the next steps of our amazing journey together to begin.

Dedication

Dedicated to my beloved family.

Chapter 1

Introduction

The development of intense, ultrafast lasers has influenced science and technology significantly. From a scientific point of view, these lasers allow us to study molecular dynamics on their natural timescales [1–8]. From a technological standpoint, ultrafast lasers are being widely used in industrial and medical applications [9–11]. Half of the Nobel prize this year was awarded for chirped pulse amplification (CPA) [12], which is the basis for the operation of intense, ultrafast lasers.

Interaction of intense laser pulses with atoms and molecules is an interesting and complicated process to study. The oscillating strong electric field of a laser is of the order of 10^8 V/cm, corresponding to a peak intensity of about 10^{16} W/cm^2, which is comparable to the electric field acting on an electron in atoms or molecules. This means that one can alter the electric field that electrons are experiencing in matter by using intense lasers, which in principle can lead to the capability of controlling the outcome of a chemical reaction [1, 13, 14]. This is the idea behind quantum control of chemical reactions.

Moreover, performing time-resolved studies of the dynamics of molecules is possible using a short laser pulse due to the fact that the pulse duration of these lasers is shorter than the natural timescales of the processes to be studied. The electronic dynamics can be probed using high harmonic generation (HHG) [6], which provides attosecond pulses, while the vibrational and rotational dynamics can be probed using tens of femtosecond and picosecond

pulses, respectively.

From a theoretical point of view, due to the very strong electric field, low-order perturbation theory does not work in most cases, and high-order perturbation theory is computationally demanding. Solving the time-dependent Schrödinger equation (TDSE) for these processes is also challenging. Theoretical physicists working in this field are developing new approximate methods to solve the problem of the interaction of atoms or molecules with intense laser pulses.

In this thesis, experimental results focused on the interaction of strong field laser pulses with molecules are reported. In chapter 2, the chirp of laser pulses is used to control the formation of excited neutral D fragments from D_2. In chapter 3, three-body fragmentation of CO_2 into $C^+ + O^+ + O^+$ ionic fragments is presented. The focus of this study is on how we can distinguish the pathways in which identical O^+ fragments are formed in sequential breakup processes.

Chapter 2

Chirp dependence of the formation of excited neutral D fragments from D_2 in intense ultrafast laser pulses

2.1 Introduction

When a molecule interacts with the strong field of a laser, interesting phenomena occur [1, 15–24]. While this interaction results in ionized atoms or ionic fragments in many cases, it is possible that the atoms or molecular fragments survive the laser field in an excited Rydberg state [22, 25–28]. Studying and understanding the processes that result in the formation of excited neutral atoms or molecular fragments have attracted significant attention in the past few years [20, 22, 25–30]. One interesting example is the observation of a very large acceleration (about $10^{14}g$, where g is the Earth's gravitational acceleration) of neutral atomic fragments in intense short laser pulses [26]. As the authors of Ref. [26] state: "To our knowledge, this is by far the highest observed acceleration on neutral atoms in external (laser) fields... ."

When an atom interacts with the strong field of a linearly-polarized laser and an electron is ejected, it is possible for the electron to recollide with the atom when the direction of the

laser field flips. This rescattering process has been nicely described in Ref. [31] : "During strong-field multiphoton ionization, a wave packet is formed each time the laser field passes its maximum value. Within the first laser period after ionization there is a significant probability that the electron will return to the vicinity of the ion with very high kinetic energy". Above threshold ionization (ATI) [15], nonsequential multiple ionization (NSMI) [16], and high harmonic generation (HHG) [17] are all consequences of this rescattering process.

The formation of excited neutral fragments is widely described using the frustrated tunneling ionization (FTI) mechanism [20, 25], which is based on strong-field tunneling and rescattering [31] processes. In this case, the rescattering electron is captured by the Coulomb potential of the atom. This results in the formation of excited neutral atoms. The same argument can be used to describe the formation of excited neutral fragments from molecules [25, 27].

The FTI mechanism is not the only description of the formaion of excited neutral fragments in strong laser fields. In Ref. [32] for example, the authors argue that a multiphoton absorption may lead to the formation of these fragments. They mention that based on theoretical calculations [32, 33]: "these Rydberg atoms are formed by electrons ionized before the peak of the laser field and that rescattering does not play any role". Based on different possible mechanisms for the formation of excited neutral fragments, it seems that more work is needed to understand this process.

In this chapter, we report experimental results on the formation of excited neutral D fragments from D_2. The kinetic energy release (KER) of the D* fragments is observed to be very sensitive to the laser parameters. We implement a single-prism compressor [34], which is described in Sec 2.2.4, to control the chirp of the laser pulses that interact with the D_2 molecules, and consequently control the formation of D* fragments.

2.2 Experimental technique

In order to perform the measurements presented in this chapter, the James R. Macdonald Laboratory (JRML) laser system known as PULSAR [35], a single-prism compressor, and

an apparatus to detect the D* fragments [36] were used. In the sections below, we describe the above mentioned systems.

2.2.1 Laser system

Linearly-polarized pulses from the PULSAR laser system with a pulse duration of 23 fs, full width half maximum (FWHM) in intensity, repetition rate of 10 kHz, and central wavelength of 790 nm are used. Second harmonic generation (SHG) of the laser pulses then occurs in a beta barium borate (BBO) crystal, resulting in pulses with a central wavelength of 395 nm. The Fourier transform limited (FTL) SHG pulses have a pulse duration of about 39 fs, FWHM in intensity. The linearly-polarized SHG pulses are then focused in vacuum using a spherical mirror (f=7.5 cm), which results in a peak intensity of about 1×10^{14} W/cm^2

Before describing how the laser pulses are manipulated, Fourier transform limited (FTL) and chirped laser pulses are briefly explained in Secs. 2.2.2 and 2.2.3.

2.2.2 FTL laser pulses

One of the characteristics of a short laser pulse is that it spans tens of nanometers in bandwidth. For example, if a laser with the central wavelength of 795 nm has about 30-nm bandwidth, based on the time-energy product, $\Delta E \Delta \omega \sim \hbar$, the shortest pulse that can be delivered by the laser is 21 fs. However, a broad bandwidth does not guarantee a short pulse. For 800-nm pulses, the dispersion of almost any material, including air or optical elements along the beam path, results in a longer pulse than what is predicted by the time-energy product. This phenomenon will be explained later. Some work is usually required to get the shortest possible pulse from a broadband laser. We usually focus the laser in air using a thin converging lens and maximize the ionization of air by tweaking the laser (mainly the compressor of the laser). This is a quick test to obtain the shortest pulse. In general, the shortest pulse that a laser system can produce is called the FTL pulse.

2.2.3 Chirped laser pulses

We know that the refractive index of materials ($v = \frac{c}{n}$, where v is the speed of light in glass, c is the speed of light in vacuum, and n is the refractive index) is a function of the wavelength. In the visible region, the refractive index of most materials is larger for shorter wavelengths. For example, if red (700 nm) and blue (450 nm) light pass through the same thickness of glass, the velocity of the blue light is smaller than that of the red light.

The bandwidth of a short laser pulse spans over several tens of nanometers in wavelength. Let's assume that we start with a FTL laser pulse. If this pulse propagates through a piece of glass, the shorter wavelength components are left behind in time. This means that after propagating through glass, the longer wavelengths come first and then the shorter wavelength components arrive. This results in a positively chirped laser pulse with positive group delay dispersion, which also means that the pulse duration is longer than the FTL pulse.

Figure 2.1 shows a positively- and negatively-chirped laser pulse in the time domain. Note that in these figures, the right side is the leading edge and the left side is the trailing edge of the pulse. In Fig. 2.1(a) the right part has a longer wavelength (lower frequency) and the left hand side has a shorter wavelength (higher frequency) which corresponds to a positively chirped pulse. Figure 2.1(b) on the other hand, represents a negatively chirped laser pulse.

From a mathematical point of view, for a laser pulse passing through a medium the laser field can be written as [37]

$$E_{out}(t) = \frac{1}{2\pi} \int E_{in}(\omega) e^{i\omega t} e^{i\phi(\omega)} d\omega, \tag{2.1}$$

where $E_{in}(\omega)$ is the electric field of the pulse before the medium, $E_{out}(t)$ is the electric field of the pulse after the medium, ω is the angular frequency of the laser, L is the thickness of the material, and $\phi(\omega)$ is the phase accumulated by the pulse due to propagation in the medium. $\phi(\omega)$ can be explicitly given by

$$\phi(\omega) = \beta(\omega) L, \tag{2.2}$$

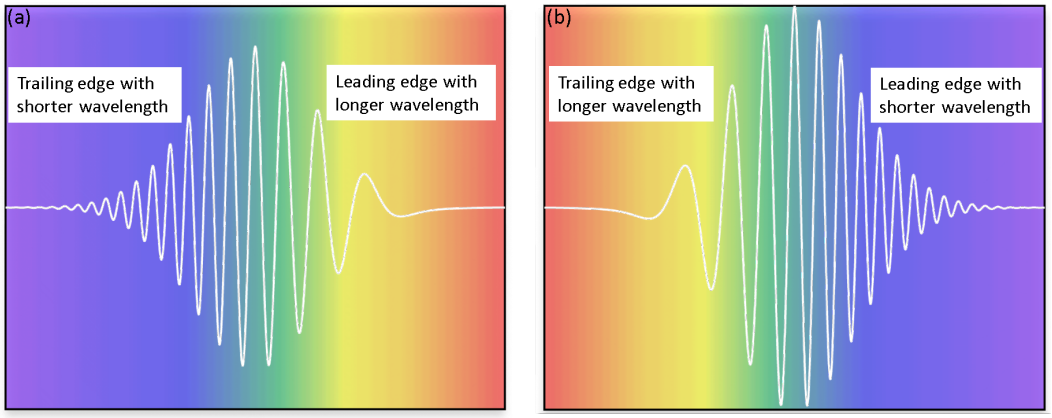

Figure 2.1: Positively- and negatively-chirped laser pulses. (a) A positively-chirped laser pulse. The low frequency components (longer wavelength) are at the leading edge of the pulse while the high frequency components (shorter wavelength) are at the trailing edge of the pulse. (b) A negatively-chirped laser pulse. The high frequency components (shorter wavelength) are at the leading edge of the pulse while the low frequency components (longer wavelength) are at the trailing edge of the pulse.

where $\beta(\omega) = \frac{2n\pi}{\lambda_0}$ is the propagation constant (n is the refractive index and λ_0 is the central wavelength in vacuum). The propagation constant, $\beta(\omega)$, can be written as a Taylor series around ω_0 (the central angular frequency of the laser pulse) as

$$\beta(\omega) = \beta_0 + \beta_1(\omega - \omega_0) + \frac{1}{2!}\beta_2(\omega - \omega_0)^2 + \frac{1}{3!}\beta_3(\omega - \omega_0)^3 + ... \tag{2.3}$$

It is easy to see that β_0 is the absolute phase and is the same in the time and frequency domain, while β_1 results in a shift in time. The second order term, the group velocity dispersion (GVD), β_2, on the other hand, results in a time dependent frequency in the time domain, which means that the laser pulse is linearly chirped. Multiplying the GVD by the length of the material that the pulse is propagating through results in the group delay dispersion (GDD) in fs^2. The third order term, β_3, results in third order dispersion (TOD) in the time domain. Higher order terms in the Taylor series expansion of $\beta(\omega)$ also alter the temporal shape of the laser pulse [37, 38].

2.2.4 Manipulating the GDD of laser pulses

As mentioned above, most materials introduce positive chirp to the laser pulses in, and close to, the visible region. In order to generate FTL or negatively-chirped laser puses in the visible region, chirped mirrors [39], gratings [40] or prism-based compressors [41] are used. Each of these methods has its own advantages and disadvantages. Using chirped mirrors is by far the easiest way to compensate positive chirp, however, chirp mirrors are relatively expensive, and they introduce high laser power loss. A grating compressor is cheaper, but it has the same issue of relatively high laser power loss. On the other hand, prism compressors are cost effective and have low losses if highly reflective mirrors are used for the desired wavelength range. The disadvantage of prism compressors is that one cannot compensate higher-order dispersion using such an apparatus.

In this study, a single-prism compressor [34] is implemented to manipulate the GDD of the laser pulses. The design of the single-prism compressor, which is very similar to the one presented in Ref [34], is shown schematically in Fig. 2.2. After the pulses propagate through the prism the first time, they are reflected off a corner cube. A corner cube is composed of three mirrors that change the height of the beam and flip the spatial order of the colors. Moreover, the input and output beams propagate parallel to each other in opposite directions. After the corner cube, the laser light passes through the prism for the second time.

A roof mirror is then used to change the height of the laser beam before going through the prism for the third time. Also, before the fourth path through the prism, the corner cube flips the order of the colors one more time (see Fig.2.2). One can think of a single-prism compressor as a four-prism compressor which has been folded twice. The biggest advantage of this configuration is that the alignment process is much faster.

The efficiency of the single-prism compressor implemented here is about 50%, mainly due to the low reflectivity of the corner cube used in the setup. Using a corner cube with higher reflectivity can increase the overall efficiency significantly (to an estimated value of about 90%). Although the efficiency of the implemented prism compressor is rather low, it

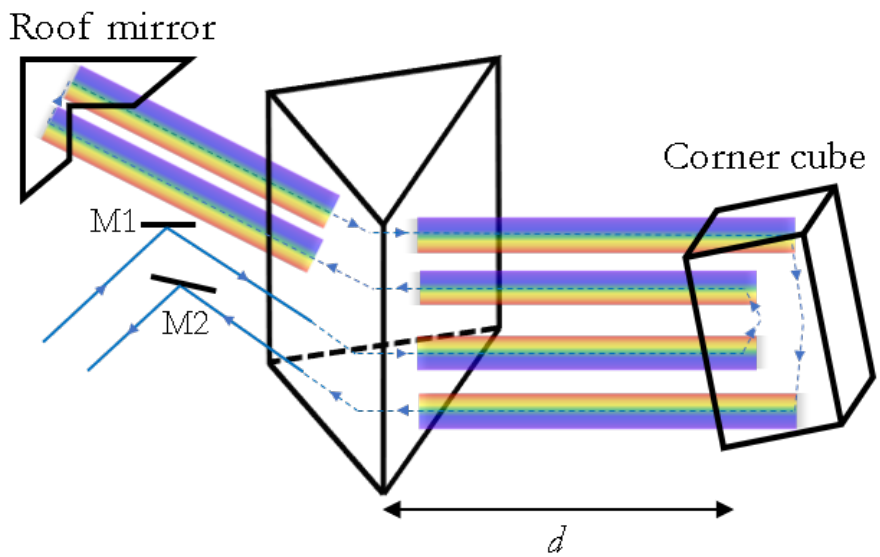

Figure 2.2: Schematic diagram of the single-prism compressor, adapted from Ref. [34], where M1 and M2 are UV enhanced flat mirrors. The corner cube flips the color order spatially and changes the height of the beam. The roof mirror only changes the height of the beam. The equilateral prism ($50\times50\times50$ mm^3) used in our setup is made of UV fused silica.

is more cost effective than using chirped mirrors for our purpose and also makes it easier to introduce the desired GDD.

The GDD of the pulses can be manipulated by changing the distance between the corner cube and prism, which is labeled d in Fig. 2.2. In our measurements, we control the GDD of the laser pulses from -1300 fs^2 to 2000 fs^2, i.e. from 110 fs negatively chirped to 150 fs positively chirped laser pulses, respectively (see Fig. 2.3). Also, it is possible to tweak the central wavelength of the pulses by rotating the prism [34]. To characterize the laser pulses, a home built self-diffraction frequency resolved optical gating (SD- FROG) [42] setup is used. The pulse characteristics are found by retrieving the phase information and calculating the GDD from the SD-FROG data. These characterized pulses are sent to the chamber where they interact with D_2 molecules introduced as an effusive jet.

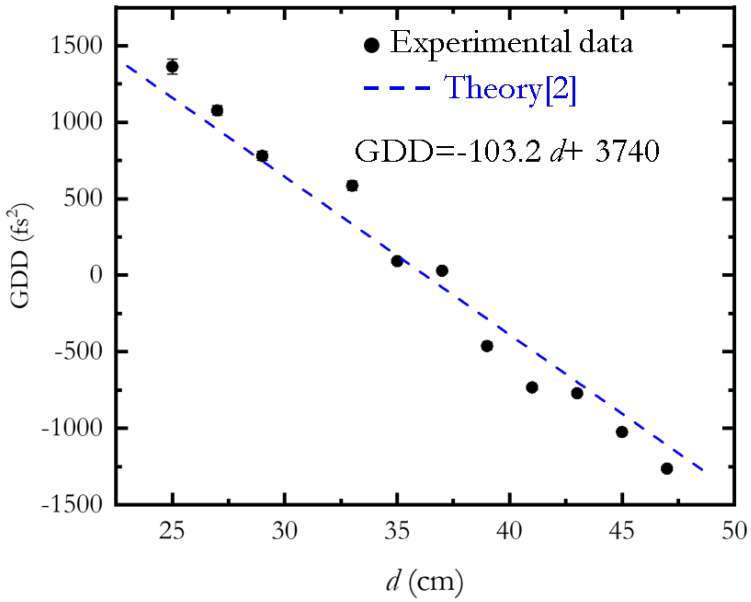

Figure 2.3: The GDD evaluated from the retrieved phase of the SD-FROG traces as a function of the distance between the cornercube and prism, d. The blue dashed line is the theoretical calculation [43].

2.2.5 Detection of excited neutral fragments

The apparatus used for measuring the time-of-flight of the neutral fragments, which was originally designed for other purposes [36], is shown in Fig. 2.4. It consists of two microchannel plate (MCP) detectors [45], but only one of the detectors is used in this study. Two high transmission meshes are located in front of each MCP detector. Mesh 1 is grounded, and a positive voltage is applied to mesh 2 in order to repel positive ions. A negative voltage is applied to the front plate of the MCP in order to repel the electrons.

The time-of-flight (TOF) of the D* fragments is measured relative to a start signal produced by reflecting a small fraction of the laser onto a photodiode. The KER reported here is lower than the actual KER of the fragmentation process as we are not measuring the transverse energy that fragments gain with respect to the TOF axis, i.e. z axis. For calculating KER we find the velocity of the fragments in the z direction, v_z

$$v_z = \frac{l - z_0}{TOF}, \tag{2.4}$$

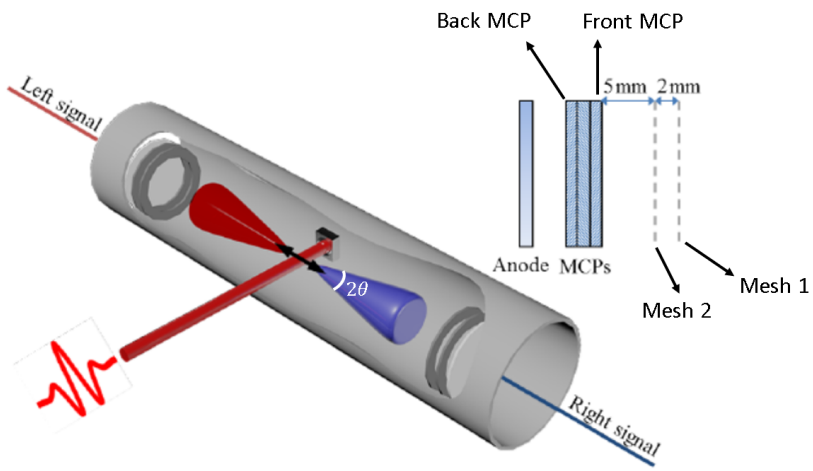

Figure 2.4: Schematic diagram of the apparatus used to detect neutral D fragments adapted from Ref. [44]. The acceptance angle, 2θ, is about 15°, which is calculated based on the geometry of the setup (see text).

where l is the distance between the origin of the z-axis and the detector, and z_0 is the position of the laser focus with respect to the origin. So, $l - z_0$ is the distance between the laser focus and the detector. The KER is then calculated using:

$$KER = 2 \times \frac{1}{2} m v_z^2, \tag{2.5}$$

where m is the mass of the fragments (D* in this case). Note that the KER is twice the kinetic energy of one of the fragments. To estimate the transverse kinetic energy, we notice that

$$\tan\theta = \frac{r_D}{l - z_0} = \frac{v_T}{v_z}, \tag{2.6}$$

where 2θ is the cone angle shown in Fig. 2.4, r_D is the radius of the MCP detector, and v_T is the transverse velocity of the fragments. Based on the geometrical design of our setup, we estimate this transverse energy to be up to 5% of the measured KER.

For the excited neutral fragments to be detected, their internal energy should be higher than the work function of the MCP, which is about 5 eV [45]. This internal energy is

then transferred to the detector through different possible mechanisms [44], liberating an electron(s) from the MCP which starts an electron avalanche [45]. In the case of the formation of D* fragments, any excited D with $n \geq 2$ can be detected, since the internal energy is $\geq 10.2eV$, which is greater than the work function of an MCP.

2.3 Results and discussion

2.3.1 Results

In Fig. 2.5, which shows the KER of D* fragments generated in the interaction of D_2 molecules and 395 nm FTL laser pulses, two distinct peaks are present. The high KER peak is associated with the $D_2 \rightarrow D^+ + D^*$ breakup according to Ref. [25]. The authors of this paper report a correlation between the kinetic energy distribution of H* and H^+ fragments which suggests that these fragments originate from the same molecule, i.e. $H^+ + H^*$ breakup. Furthermore, a Coulomb explosion followed by recombination of one of the rescattering electrons was suggested as the underlying mechanism [25]. The low KER peak is attributed to the $D_2 \rightarrow D^* + D$ fragmentation process [22, 25].

In order to study the dependence of D* formation on the chirp of the laser pulses, we first conduct the measurements with positively chirped laser pulses. Figure 2.6 shows the KER of D* fragments for a few positively chirped laser pulses. In all of the KER distributions showed from now on, the KER values are scaled to match the high-KER peak (peak 3).

One can see that by increasing the GDD of the laser pulses, the structure of the KER distribution of the fragments resulting from $D_2 \rightarrow D + D^*$ process is changing. In Fig. 2.6, we call the peak centered around 1 eV "peak 1". By increasing the positive chirp of the pulses, peak 1 is suppressed. Moreover, a peak centered around 2 eV, denoted "peak 2", starts appearing at higher values of positive chirp. This suggests a control of the branching ratio of peaks 1 and 2 by adding positive GDD to the laser pulses. However, it is not possible to separate the effect of the pulse duration from that of the chirp just by chirping the pulses in one direction. Additionally, because the measurements are conducted at constant fluence of

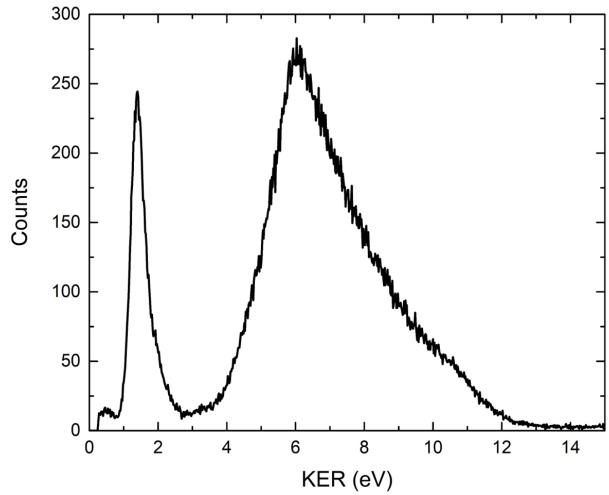

Figure 2.5: The KER associated with D* fragments produced by 39 fs (FTL) laser pulses with a central wavelength of about 395 nm. The peaks with high and low KER are associated with the $D_2 \rightarrow D^+ + D^*$ and $D_2 \rightarrow D^* + D$ fragmentation processes, respectively (see text and Refs. [22, 25]).

the laser, one cannot separate the effect of the chirp from that of the peak intensity of the pulses by chirping the pulses in one direction.

In order to disentangle the chirp dependence from pulse duration and peak intensity that might play a role in the observed phenomenon, we perform additional measurements as a function of the added positive or negative GDD to the laser pulses by employing the single-prism compressor described earlier. In Fig. 2.7 (a) and (b), peak 1 is shown for chirped pulses with ± 700 fs^2 and about ± 1400 fs^2 GDD, respectively. It is evident from Fig. 2.7 that peak 1 is suppressed more by positively-chirped pulses compared to negatively-chirped laser pulses. This shows that there is a chirp dependence of fragmentation events recorded in peak 1, i.e. D+D* with KER $\sim$ 1 eV.

To better quantify this chirp dependence, we define the branching ratio, BR, of peak 2 as

$$\mathrm{BR} = \frac{\mathrm{M}(2)}{\mathrm{M}(1)+\mathrm{M}(2)}, \tag{2.7}$$

where $M(1)$ and $M(2)$ are the measured number of events in peak 1 and peak 2, respectively. In order to find the BR at different GDD values, a peak fitting method is used, as shown

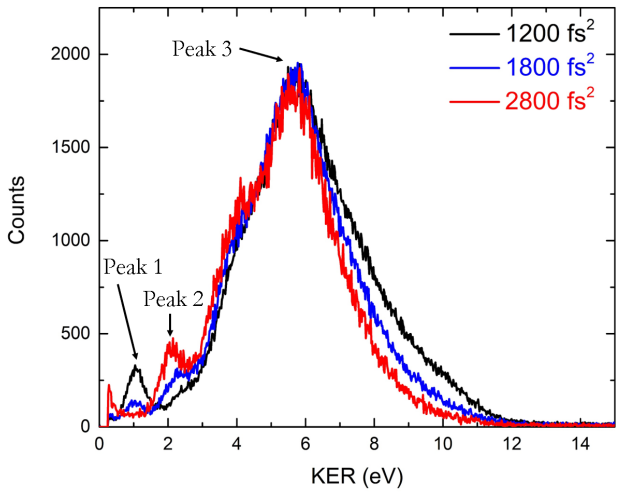

Figure 2.6: The KER associated with D* fragment production by laser pulses having positive chirp. By increasing the GDD, peak 1 is suppressed while peak 2 is enhanced. Note that the KER distributions for different GDD values are scaled to match the high-KER peak (peak 3).

in Fig. 2.8. First, we subtract the low-KER tail of peak 3 to better evaluate peak 1 and peak 2. To do so, a Gaussian function is fitted to the low energy tail of peak 3, over a range marked in Fig. 2.8.(a) by the two blue dashed vertical lines. Then this Gaussian function is subtracted from the low-KER region resulting in Fig. 2.8.(b). After the subtraction, two Gaussian functions are fitted to the low-KER peaks yielding the number of events in peak 1 and peak 2. This procedure is repeated for each GDD value, and the results are used to calculate the BR shown in Fig. 2.9.

Figure 2.9 shows the BR as a function of GDD of the laser pulses. Due to the complexity of finding the error of GDD retrieved from the FROG algorithm, the error in GDD is found by running the retrieval algorithm multiple times and the standard deviation is used as an error estimate.

If the BR depends on the chirp of the laser pulses, a difference in BR between positively- and negatively-chirped laser pulses by the same amount is expected. As can be seen from Fig 2.9, there is a significant difference in the branching ratio between positive and negative GDD laser pulses in comparison to the experimental errors at each GDD. This confirms that

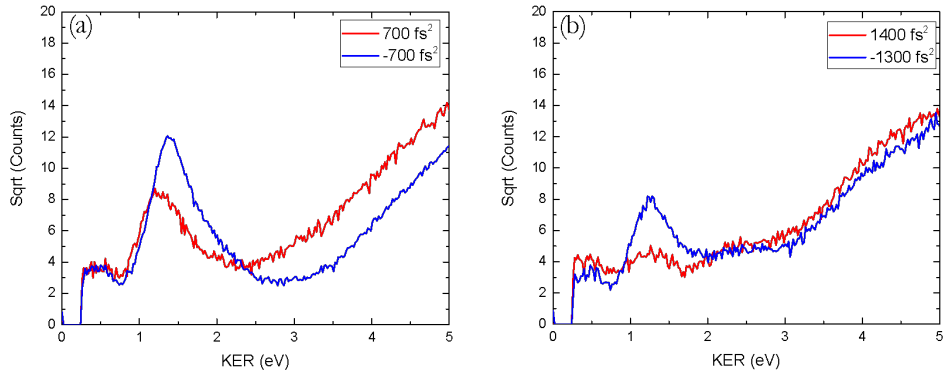

Figure 2.7: The KER associated with D* fragments produced by (a) $\pm$ 700 fs^2 and (b) $\pm$ 1400 fs^2 chirped pulses.

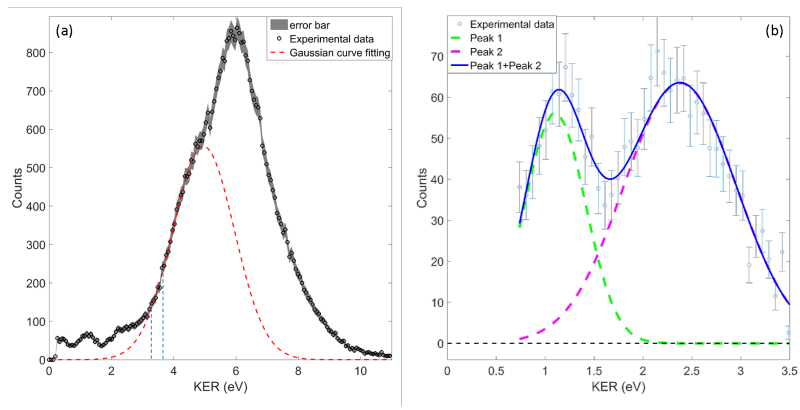

Figure 2.8: Peak fitting procedure to find the branching ratios (see text). (a) fitting a Gaussian to subtract from the low KER region. (b) result of the peak fitting after subtraction.

we are observing a chirp dependence and not just a pulse duration or intensity dependence.

2.3.2 A qualitative description of the experimental observation

As mentioned in Sec. 2.1, the formation of excited neutral fragments is widely described using the frustrated tunneling ionization (FTI) model. In this model, the tunnel-ionized electron is captured by the Coulomb potential of the atom (or molecule) which results in the formation of excited neutral atoms (or molecular fragments) [20, 25]. There are two reasons supporting the FTI model's description of the formation of excited neutral atoms or fragments. One reason is the similarity of the KER distribution of H^+ and H^* generated from H_2 [25]. The

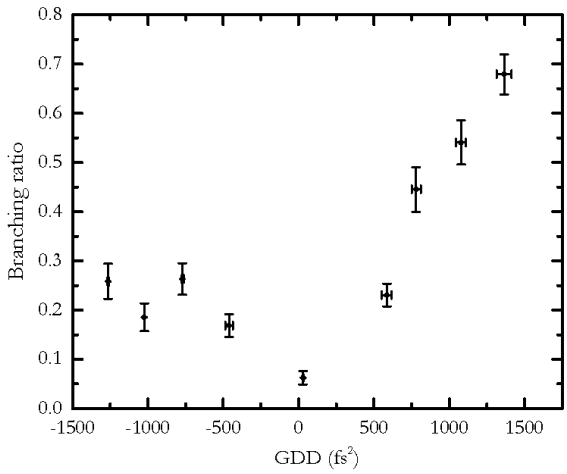

Figure 2.9: The BR defined in Eq. 2.7 as a function of the GDD. Note that the behavior of the BR is significantly different for laser pulses with positive and negative GDD.

other reason is the strong dependence of the yield of excited neutral atoms [20] or fragments [22, 25] on the laser polarization. Specifically, changing the laser polarization from linear to circular significantly suppresses the yield of the excited neutral atoms or fragments. This suggests that rescattering, which also has a similar strong polarization dependence, may be a reason for the formation of these fragments in Rydberg states. As discussed earlier, FTI is not the only model that can be used to describe the formation of excited neutral fragments.

In order to describe the chirp dependence reported here theoretical calculations, based on the FTI model or other mechanisms, are required. In such calculations, the chirp of the laser pulses should be included; however, it is not clear to us how the chirp of the pulses can affect the outcome within the FTI model.

Regardless of the model used, we look at the potential energy curves (PECs) of H_2 [46], shown in Fig. 2.10, which are similar to the ones for D_2, to identify the likely pathways for D^++D^* formation. In identifying the pathways, we should keep in mind that the ground state of H_2 is the singlet $^1\Sigma_g^+$ state, and the final state should also be singlet as the laser does not change the spin. Formation of fragments with a KER of about 1 eV (peak 1) is most likely associated with a five-photon absorption. The D_2 molecule absorbs five 390 nm photons, schematically shown by the five blue dashed arrows in Fig. 2.10, populating states

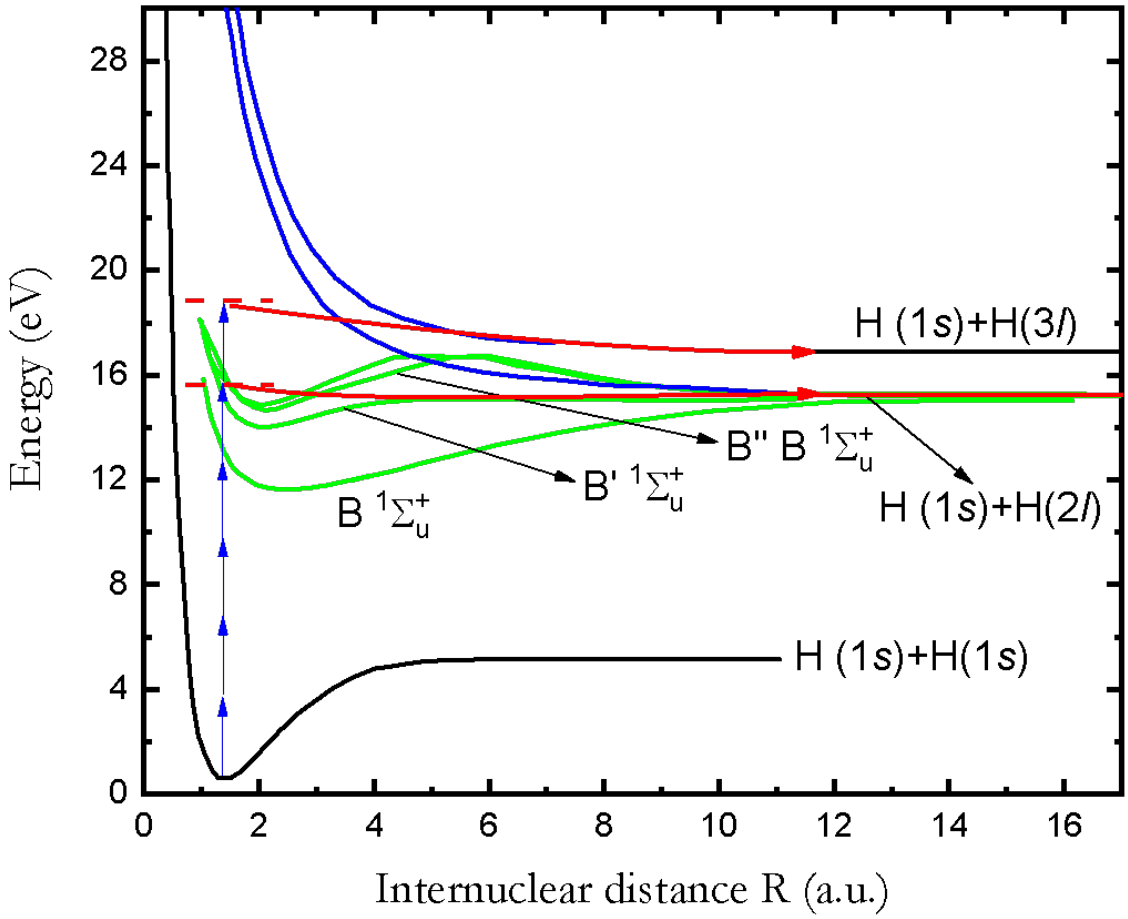

Figure 2.10: Some PECs of H_2 adapted from Ref. [46]. Two possible pathways for the formation of D* fragments are indicated by the five and six blue arrows depicting five- and six- photon absorption (see text). The horizontal red and black lines show the D($2l$)+D($1s$) and D($3l$)+D($1s$) dissociation limits, respectively.

like B $^1\Sigma_u^+$, B′ $^1\Sigma_u^+$, and B″ B $^1\Sigma_u^+$ or others. Then, the D_2 molecule undergoes dissociation through one of the nQ_1 states into D($2l$)+D($1s$), which results in a KER of ∼1 eV. Note that parity selection rules are obeyed, as the transition occurs by absorbing an odd number of photons, and the states involved have opposite parity to the H_2 ground state.

The formation of D* fragments with a KER peak of about 2 eV occurs by absorbing six photons and dissociating into the D(n=3)+D($1s$) limit, shown in Fig. 2.10. Selection rules require that the states involved have the same parity as the H_2 ground state when an even

number of photons are absorbed. As a result, the B states shown in Fig. 2.10 cannot be populated by absorbing six photons. There are a few states that can be populated in this process, for example E,F $^1\Sigma_g^+$, H $^1\Sigma_g^+$, and O $^1\Sigma_g^+$ [47], none of which are shown in Fig. 2.10

From the discussion above, it is clear that there are a few states that can be populated by five- or six-photon transitions and dissociate into D($2l$)+D($1s$) or D(n=3)+D($1s$), respectively . We thus expect interference between different pathways to be the reason for the observed chirp dependence that modulates peak 1 and peak 2. However, it is not clear how the chirp of the pulses affects the interference between different pathways. The description presented here is qualitative, and theoretical calculations are required to better understand the D* formation and its chirp dependence.

2.4 Summary

The formation of excited neutral D (i.e. D*) fragments from D_2 molecules interacting with the strong field of a laser at the 395 nm central wavelength exhibits strong chirp dependence. The experimental results indicate that the low KER distribution is very sensitive in this case to the chirp of the laser pulses, especially for positive chirp.

Chapter 3

Native frames: Imaging three-body breakup involving two identical fragments

3.1 Introduction

Understanding the fragmentation process of polyatomic molecules is challenging from two different aspects. First, conducting experiments on such molecules is complicated if three or more fragments are to be detected in coincidence with each other. The development of imaging techniques has made it possible to study three- or four-body fragmentation processes experimentally [48, 49]. The other challenge is how to analyze and visualize the multidimensional data to understand the dynamics of the fragmentation process. Developing analysis methods that facilitate the understanding of fragmentation of polyatomic molecules has been an ongoing effort, for example see Refs. [50–56]. Specifically, one important question is whether we can separate the concerted fragmentation processes from the sequential breakup. In a concerted breakup, both bonds of an ABC molecule break at the same time. On the other hand, in sequential breakup one of the bonds breaks first, for example the A-B, bond. The intermediate BC molecule breaks in the second step after a time τ. Two well-known

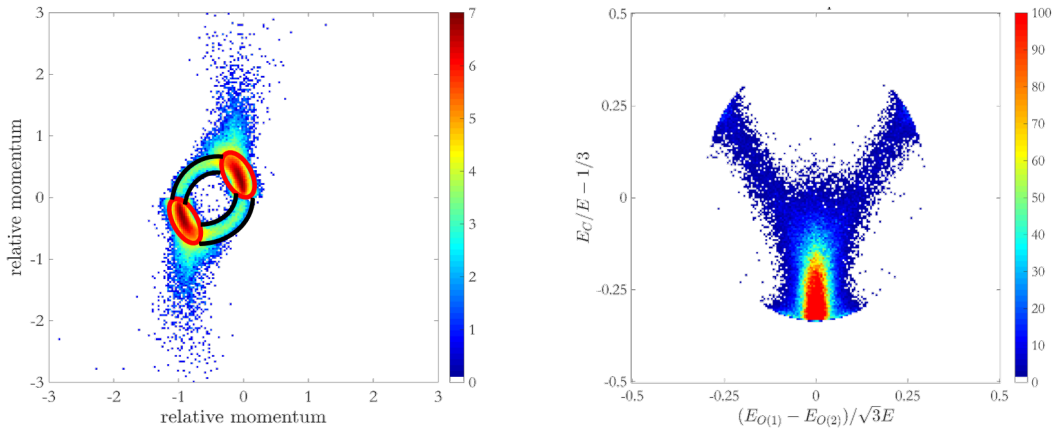

Figure 3.1: (a) Newton diagram: the momentum of the three fragments is calculated and normalized to one of the calculated momenta (here normalized to the momentum of one of the O^+ fragments). (b) Dalitz plot: shows the energy sharing between the three fragments. E is the total energy of the fragments

analysis methods used to identify concerted and sequential fragmentation events are Newton diagrams [51, 53, 55] and Dalitz plots [51, 53–55]. In Fig. 3.1(a) and (b) we show the Newton diagram and Dalitz plot of three-body fragmentation of CO_2 into C^++O^++O^+, respectively. The ring like structure in Fig. 3.1.(a) has been used to identify sequential events associated with intermediate CO^{2+} that rotates for a long time compared to its rotational period. These sequential events, separated from concerted ones, are within the two black "boxes" in Fig 3.1.(b). While these powerful methods can help identify concerted and sequential events, neither of them allow for complete separation of concerted and sequential fragmentation processes [57]. Moreover, generalizing these methods to fragmentation processes involving more than three fragments is not trivial. We recently developed the native frames method, which allows us to separate concerted from sequential fragmentation processes [57, 58].

In this chapter, the native frames method is used to study strong-field fragmentation of CO_2 into C^++O^++O^+ following triple ionization as an example of three-body breakup involving two identical fragments. This process can happen through concerted- or sequential-breakup mechanisms. In concerted breakup, the two O^+ fragments play indistinguishable roles. In sequential breakup, however, one of the O^+ fragments originates from the first fragmentation step of the transient ${CO_2}^{3+}$, and the other one originates from unimolecular

dissociation of the intermediate CO^{2+} in the second step. Therefore, in sequential breakup the paths taken by the two O^+ fragments can be distinguished.

3.2 Experimental technique

Three-body fragmentation of CO_2^{3+} into C^++O^++O^+ is measured using the cold target recoil ion momentum spectroscopy (COLTRIMS) technique [59–61]. Figure 3.2 shows a schematic of the COLTRIMS apparatus. Only ions are detected in the current experiment. The position and time-of-flight (TOF) of the ionic fragments are measured in coincidence, which allows us to retrieve the complete three-dimensional momentum of all of them.

We also measure the two-body breakup of CO_2^{3+} into CO^{2+}+O^+. This channel corresponds to the case when only the first step of the sequential breakup of CO_2^{3+} happens, which means that the intermediate CO^{2+} dication arrives intact to the detector [57].

In our coincident measurement of the C^++O^++O^+ channel, one of the O^+ fragments is detected as a second hit and the other as a third hit on the detector. This detection time order does not provide us with any information related to the three-body fragmentation analysis. For this reason, we randomize the detection time order, i.e. (x, y, t) of the O^+ fragments.

Linearly-polarized laser pulses are focused on a CO_2 supersonic jet using a spherical mirror (f=75 mm) to initiate the fragmentation process by triply ionizing the CO_2 molecules. The JRML PULSAR laser system [35] with a central wavelength of 790 nm and repetition rate of 10 kHz is used in our experiment. The typical pulse duration of the PULSAR laser, FWHM in intensity, is 23 fs, which is measured using the second harmonic frequency resolved optical gating (SHG FROG) technique [63].

The peak intensity is determined to be about 6.7×10^{14} W/cm^2, using the kink in the momentum distribution of Ne^+ recoil ions along the laser polarization axis, p_z. This kink in p_z is related to $2U_p$ (U_p is the ponderomotive energy), from which the peak intensity is evaluated [64].

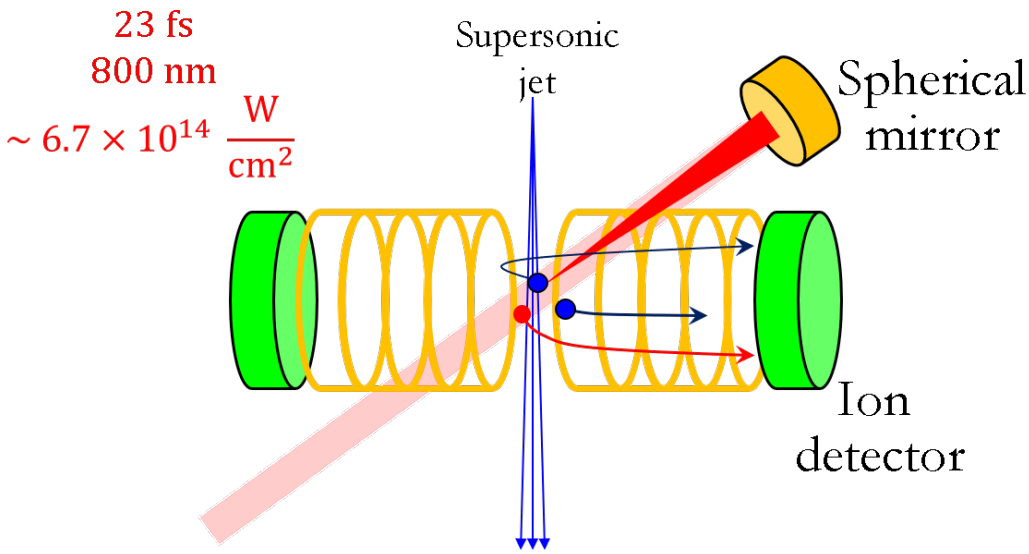

Figure 3.2: Schematic diagram of a COLTRIMS setup. Adapted from Ref. [62].

3.3 Native-frames analysis method

Recall that three-body sequential breakup happens in two steps. As an example, let's assume that in the first fragmentation step of an arbitrary AB_2 molecule, it breaks into AB^{2+}+B^+ fragments. The second fragmentation step, i.e. $AB^{2+}\rightarrow A^+$+B^+, is assumed to happen after the AB^{2+} intermediate molecule rotates for a long time (before it dissociates) compared to its rotational period. As mentioned before, the fragmentation process is detected as a sequential breakup if this assumption is valid. The data is analyzed in the center of mass frame of the first and second steps that are the two native frames of the fragmentation process.

We use Jacobi coordinates [65] and relative momenta, shown in Fig 3.3 for an arbitrary AB_2 molecule, to reduce dimensionality of the three body problem [65]. The coordinate choice in this figure assumes sequential breakup with a $AB_(1)$ intermediate molecule. The two identical fragments are "labeled" $B_{(1)}$ and $B_{(2)}$. This "labeling" will be discussed later on. Either $B_{(1)}$ or $B_{(2)}$ may originate from the second fragmentation step. We only present the case in which $B_{(1)}$ originates from the second step to introduce the method as the other case follows a similar procedure. The fragments' momenta $\vec{P}_A$, $\vec{P}_{B_{(1)}}$, and $\vec{P}_{B_{(2)}}$ are evaluated in the CO_2^{3+} frame.

Then, following Ref. [58], we write the relative momentum of A with respect to $B_{(1)}$,

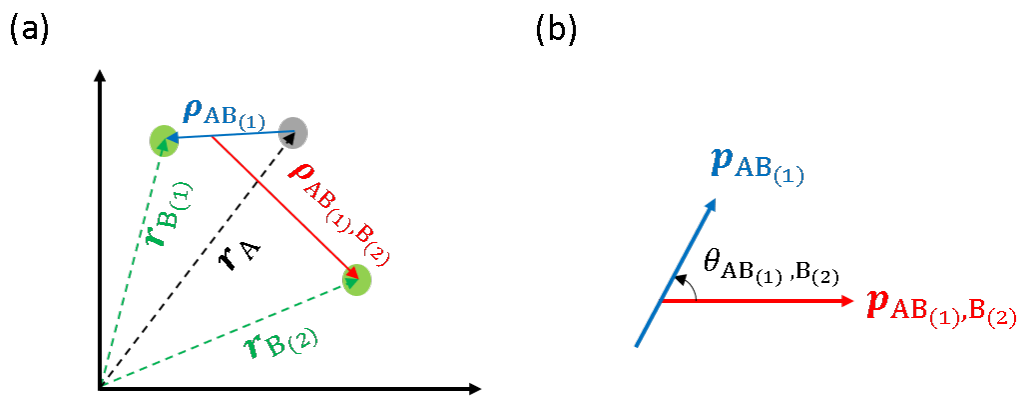

Figure 3.3: Jacobi coordinates and how they are used to analyze the data in the native-frames method. (a) Schematic of Jacobi coordinates. (b) Relative momenta and $\theta_{AB_{(1)},B_{(2)}}$ defined using the Jacobi coordinates in (a) (see text). Adapted from Ref. [58].

$\vec{p}_{AB_{(1)}}$, and the relative momentum of $B_{(2)}$ with respect to the center of mass of the $AB_{(1)}$ intermediate dication, $\vec{p}_{AB_{(1)},B_{(2)}}$, as

$$\vec{p}_{\mathrm{AB}_{(1)},\mathrm{B}_{(2)}} = \frac{m_{\mathrm{AB}}}{M}\vec{P}_{\mathrm{B}_{(2)}} - \frac{m_{\mathrm{B}}}{M}\left(\vec{P}_{\mathrm{A}} + \vec{P}_{\mathrm{B}_{(1)}}\right), \tag{3.1}$$

$$\vec{p}_{\mathrm{AB}_{(1)}} = \mu_{\mathrm{AB}}\left(\frac{\vec{P}_{\mathrm{B}_{(1)}}}{m_{\mathrm{B}}} - \frac{\vec{P}_{\mathrm{A}}}{m_{\mathrm{A}}}\right), \tag{3.2}$$

where, m_{AB}=m_A+m_B, M=m_A+2 m_B, and $\frac{1}{\mu_{AB}} = \frac{1}{m_A} + \frac{1}{m_B}$. The angle between $\vec{p}_{AB_{(1)},B_{(2)}}$ and $\vec{p}_{AB_{(1)}}$ is defined as

$$\theta_{\mathrm{AB}_{(1)},\mathrm{B}_{(2)}} = \arccos\left(\frac{\vec{p}_{\mathrm{AB}_{(1)},\mathrm{B}_{(2)}} \cdot \vec{p}_{\mathrm{AB}_{(1)}}}{|\vec{p}_{\mathrm{AB}_{(1)},\mathrm{B}_{(2)}}||\vec{p}_{\mathrm{AB}_{(1)}}|}\right). \tag{3.3}$$

If the intermediate dication rotates for a long time compared to its rotational period before dissociating, the $\theta_{AB_{(1)},B_{(2)}}$ distribution, $N(\theta_{AB_{(1)},B_{(2)}})$, is expected to form a uniform distribution [57, 58]. Note that $\theta_{AB_{(1)},B_{(2)}}$ is used to analyze the data in the native frames because this three-body fragmentation processes is assumed to happen in the fragmentation plane [57, 58]. To support this assumption and determine how much angular momentum is gained by the intermediate dication, we simulate the first step of the three-body fragmentation of CO_2^{3+}, i.e. the breakup into O^++CO^{2+}, classically. This simulation is explained below.

3.3.1 Classical Coulomb explosion simulation

As stated above, one of the assumptions of the native-frames analysis method is that the intermediate $AB_{(1)}$ molecule, produced in the first step of sequential fragmentation, rotates in the fragmentation plane resulting in a uniform angular distribution $N(\theta_{AB_{(1)},B_{(2)}})$ of the unimolecular dissociation. If the intermediate $AB_{(1)}$ fragment gains large amounts of angular momentum perpendicular to the fragmentation plane, then we can argue that the rotation is in the fragmentation plane. To estimate how much angular momentum is gained by the intermediate dication, we perform a classical Coulomb-explosion simulation of the sequential breakup of CO_2^{3+}.

Figure. 3.4 shows a schematic diagram of the initial conditions used in the simulation. We use the C–O equilibrium distance of the neutral CO_2 molecule from the NIST database, $R_{CO} = 1.162$ Å. On the other hand, the bond angle ξ_i, which is 180 degrees for the equilibrium geometry of CO_2, is used as a parameter. For the equilibrium configuration, the O^+ fragment does not apply any torque on the CO^{2+} fragment, and the CO^{2+} does not gain angular momentum perpendicular to the fragmentation plane. If the CO_2 molecule is bent, however, the CO^{2+} experiences a torque.

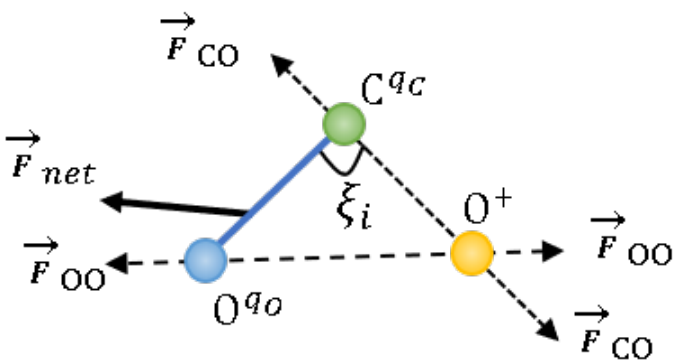

Figure 3.4: Schematic diagram of a bent CO_2^{3+}.

In order to compute the amount of angular momentum gained, we model the CO^{2+} as a rigid rotor with two point charges, q_C and q_O, separated by R_{CO}. To evaluate the charges q_C and q_O, we use the permanent dipole of the CO^{2+} ground electronic state at

$R_{\mathrm{CO}} = 1.162\,\text{Å}$ calculated to be $D \simeq 3\,\mathrm{Debye}$ [66]. For the origin defined at the CM of the CO^{2+} molecule, we approximate the dipole as

$$D = R_{\mathrm{CO}}(\delta q + \frac{1}{7}) \tag{3.4}$$

where $q_{\mathrm{C}} = 1 + \delta q$ and $q_{\mathrm{O}} = 1 - \delta q$. This results in charges of $q_{\mathrm{C}} \simeq 1.4$ and $q_{\mathrm{O}} \simeq 0.6$ a.u. Note that in calculating D, we find a term $R_{\mathrm{CO}}(m_{\mathrm{O}} - m_{\mathrm{C}})/(m_{\mathrm{O}} + m_{\mathrm{C}})$ which is equal to $R_{\mathrm{CO}}/7$, where m_{C} and m_{O} are the masses of the carbon and oxygen, respectively.

Due to the mutual Coulomb repulsion and conservation of linear momentum, the O^+ and CO^{2+} undergo back-to-back breakup, and the CO^{2+} gains angular momentum resulting in its rotation in the molecular plane. These translation and rotation motions are described by a set of coupled differential equations that we propagate in time (in steps of 1 a.u.) using the "ode45" function in MATLAB. We assume that the motion starts from rest at $t = 0$ and at the internuclear distances of the equilibrium values of the neutral molecule. The propagation of the equations of motion is terminated after 3×10^4 a.u. (or about 725 fs) when the distance between the two fragments exceeds 350 a.u., at which time the CO^{2+} velocity and angular momentum converge (at better than 0.1%). The calculated angular momentum of the intermediate CO^{2+} as a function of initial bond angle ξ_i is shown in Fig. 3.5(a). It can be seen that the final angular momentum increases rapidly with bending of the CO_2, resulting in a few tens of $\hbar$ for bending angles that are 3 degrees off equilibrium and above. Moreover, the time evolution shown in Fig. 3.5(b) indicates that this angular momentum is gained in a couple hundred femtoseconds. This is an indication that the rotation of the intermediate dication occurs in the fragmentation plane verifying the assumption needed for a uniform $N(\theta_{\mathrm{CO,O}})$.

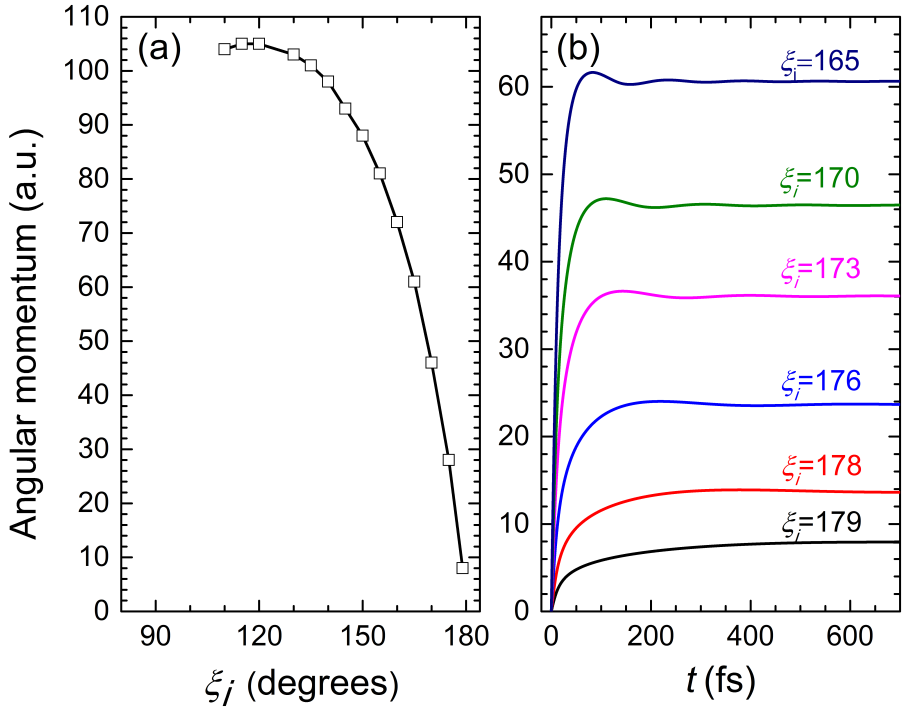

Figure 3.5: (a) Calculated final angular momentum of the intermediate CO^{2+} fragment as a function of the initial bond angle ξ_i. (b) The time evolution of the total angular momentum for a few values of ξ_i.

3.4 Results and discussion

3.4.1 Distinguishing the pathways of O^+ fragments in sequential breakup

An interesting question in three-body breakup involving identical fragments is whether the pathways that these identical fragments go through can be distinguished from each other. For the case of CO_2 (O=C=O), as an example of a symmetric molecule, it is impossible to distinguish the two identical O^+ fragments in concerted breakup. In contrast, for sequential breakup, $CO_2^{3+} \rightarrow CO^{2+} + O^+ \rightarrow C^+ + O^+ + O^+$, the pathways which the O^+ fragments go through may be distinguished as they originate from different steps.

It is equally likely that either oxygen fragment originates from the first or second fragmentation step. For analyzing the data, we label the two detected O^+ fragments as $O^+_{(1)}$ and $O^+_{(2)}$ as shown schematically in Fig. 3.6. Recall that the detection time order of the two

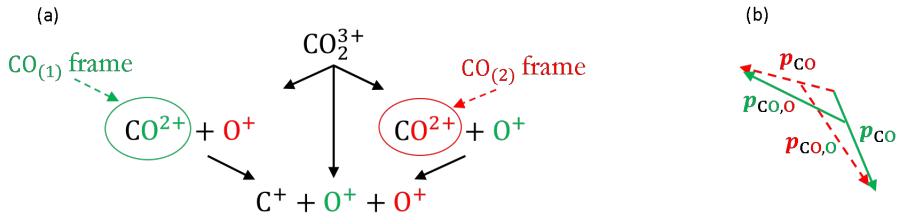

Figure 3.6: Labeling the two O^+ fragments. (a) In this figure, the $CO_{(1)}$ intermediate dication is defined if the "green" O originates from the second fragmentation step. The $CO_{(2)}$ intermediate dication is defined if the "red" O originates from the second fragmentation step. Note that color-coding the oxygens is arbitrary. (b) Relative momenta assuming $CO_{(1)}$ and $CO_{(2)}$ as intermediate dications.

oxygen fragments has been randomized, so this labeling is arbitrary. One can analyze the data assuming $O^+_{(1)}$ originates from the second step, which means that $CO^{2+}_{(1)}$ is the intermediate dication. In this case, sequential events are analyzed correctly 50% of the time. In the other 50% of the sequential events, $O^+_{(2)}$ originates from the second step, and $CO^{2+}_{(2)}$ is the intermediate dication. For this reason, we analyze the data both ways as shown in Fig. 3.7. As stated before, $N(\theta_{\mathrm{CO,O}})$ is expected to form a uniform distribution. This uniform distribution is expected only for the events in which the oxygen fragments are assigned in the correct breakup order. Such a distribution can be seen in Fig. 3.7 within the red boxes.

Let's take a closer look at Fig. 3.7. Although we label the two oxygen fragments as $O^+_{(1)}$ and $O^+_{(2)}$ for analysis purposes, there is only one intermediate dication which is CO^{2+}. As a result, we expect the $\mathrm{KER}_{CO^{2+}_{(1)}}$–$\theta_{CO^{2+}_{(1)}}$ and $\mathrm{KER}_{CO^{2+}_{(2)}}$–$\theta_{CO^{2+}_{(2)}}$ spectra to look identical within the statistical errors. Quantitatively about 4051 events are inside the red "box" in Fig. 3.7(a), and 4002 events are inside the red box in Fig. 3.7(b). This means that within the statistical error bars, 50% of the sequential events are inside each red box. The number of events in each red box slightly changes within the uncertainty each time we run the analysis code because we randomize the detection time order of the two O^+ fragments.

We now focus on the data within the red boxes. Recall that in Fig. 3.7 (a) and (b), it is assumed that $CO^{2+}_{(1)}$ and $CO^{2+}_{(2)}$ are the intermediate dications, respectively. As mentioned before, red boxes show the sequential events in which the O^+ fragments are assigned correctly. This means that for the data in the red box in Fig. 3.7 (a), $O^+_{(2)}$ is generated in

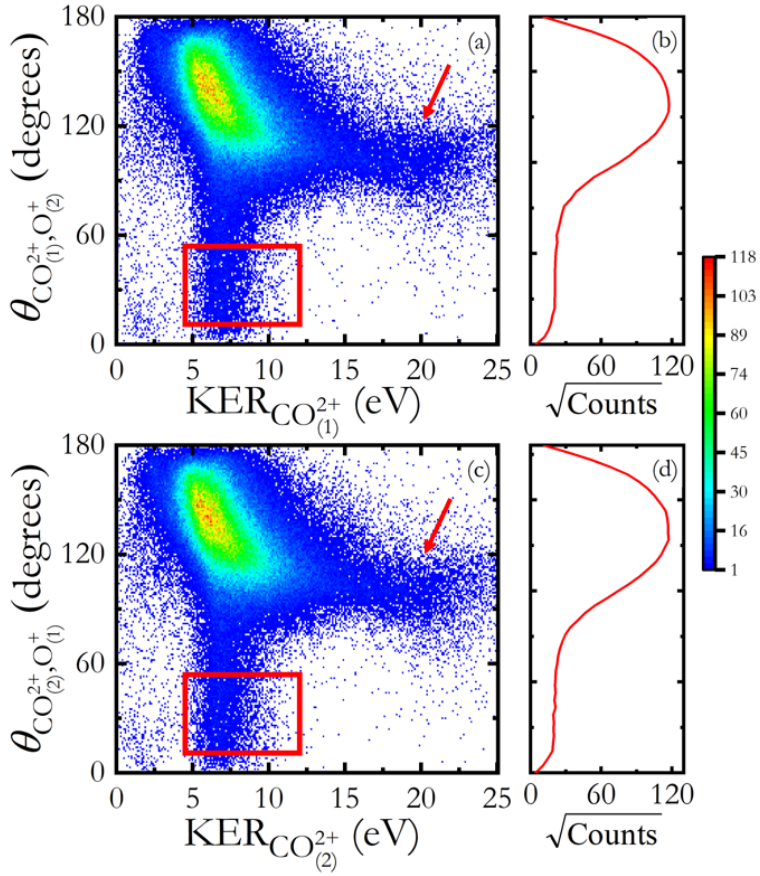

Figure 3.7: (a) Experimental data in native frames assuming $O^{+}_{(1)}$ is from the second fragmentation step. (b) $\theta_{CO^{2+}_{(1)},O^{+}_{(2)}}$ for 4.5< $KER_{CO^{2+}_{(1)}}$< 12 eV to exclude the tail shown with red arrows. (c) Same spectrum as (a) assuming $O^{+}_{(2)}$ is from the second fragmentation step. (d) $\theta_{CO^{2+}_{(2)},O^{+}_{(1)}}$ for 4.5< $KER_{CO^{2+}_{(2)}}$< 12 eV. Note that (a) and (c) look almost identical as $O^{+}_{(1)}$ or $O^{+}_{(2)}$ can originate from the first or second step. The data in the red boxes are sequential events in which the O^{+} fragments are assigned correctly.

the first fragmentation step and $O^{+}_{(1)}$ in the second. Similarly, for the data in the red box in Fig. 3.7 (b), $O^{+}_{(1)}$ originates from the first fragmentation step and $O^{+}_{(2)}$ from the second. So, the O^{+} fragments in sequential breakup are distinguished in the sense that they can be associated with the fragmentation step they are formed in. As can be seen in Fig. 3.7, part of the sequential events overlap the dominant feature which is associated with the concerted breakup. In the overlap region, we cannot say whether an event originates from concerted

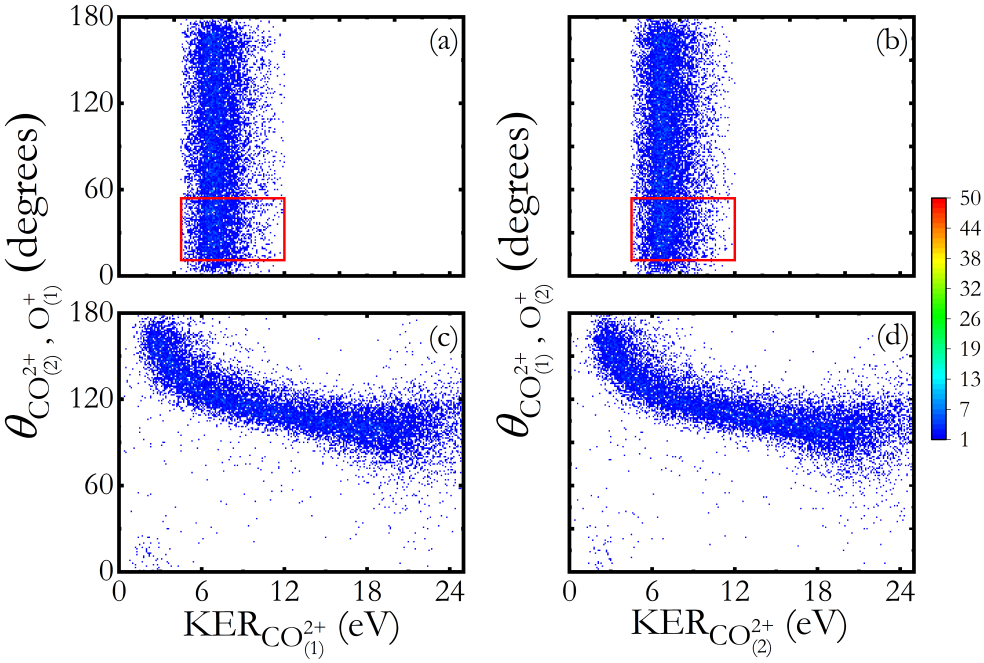

Figure 3.8: Sequential events for (a) $O^+_{(1)}$ and (b) $O^+_{(2)}$ originating from the second step. In (a) and (b), data outside the red boxes are generated using the reconstruction algorithm. (c) and (d) are the same as (a) and(b) except with the wrong order of the O^+ fragments assigned (see text).

or sequential breakup processes. We use an algorithm [58] that reconstructs breakup events equivalent to those "lost" in the overlap region and rebuild the uniform distribution over the whole range of $\theta_{CO,O}$, as shown in Figs. 3.8 (a) and (b). This algorithm takes advantage of the expected uniform distribution of $N(\theta_{CO,O})$ for sequential fragmentation processes.

The result of analyzing the reconstructed sequential events with assigning the wrong order to the O^+ fragments is shown in Figs. 3.8 (c) and (d). For example, in Fig. 3.8 (c) $O^+_{(2)}$ originates from the second fragmentation step but in analysis we assume it is formed in the first fragmentation step. These figures show that the tails of the spectrum in Fig. 3.7, indicated by the red arrows, are due to sequential breakup events in which the O^+ fragments are associated with the incorrect fragmentation step.

We demonstrated above that we can assign the O^+ fragments correctly to their breakup step. Moreover, by using the correct and incorrect assignments of sequential breakup, shown

in Figs. 3.8 (a) and (c), we can separate the concerted spectra by simple subtraction of the sequential spectra from the same spectra containing all events. For example, we subtract Figs. 3.8 (a) and (b) from Fig. 3.7 [58].

3.4.2 $\mathrm{KER_{CO}}$ in the second step

To understand the sequential fragmentation process in more detail, we identify possible states of the intermediate CO^{2+} that play a role in the sequential breakup process. In Ref. [57], $\mathrm{KER_{CO}}$ in sequential breakup of the OCS molecule, $\mathrm{OCS^{3+}} \rightarrow \mathrm{CO^{2+}} + \mathrm{S^{+}} \rightarrow \mathrm{O^{+}} + \mathrm{C^{+}} + \mathrm{S^{+}}$, is discussed in detail. Figure. 3.9 shows a comparison between $\mathrm{KER_{CO^{2+}}}$ of OCS and CO_2. This figure suggests that in sequential three-body breakup of CO_2 and in sequential breakup of OCS with CO^{2+} intermediate, the same states of CO^{2+} are populated.

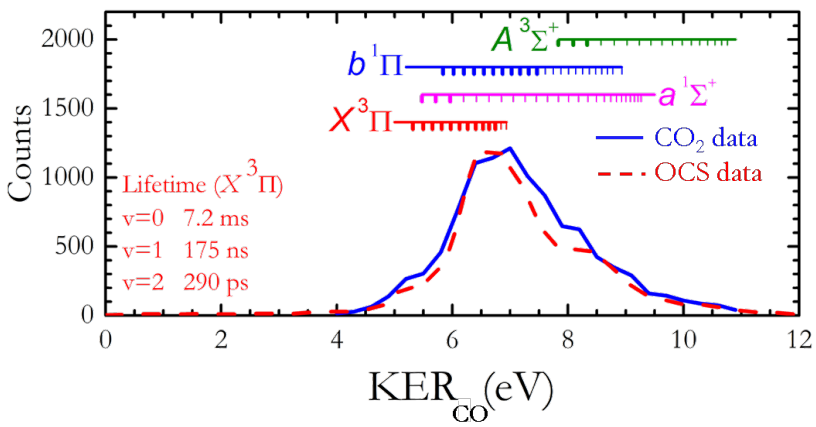

Figure 3.9: Adapted from Ref. [58]. The $\mathrm{KER_{CO}}$ distribution of the second fragmentation step of CO_2 and OCS molecules via a CO_2^{2+} intermediate dication. Note that the two spectra are very similar. The thick tick marks for different states of CO^{2+} are based on high-precision measurements and measured photoionization energies [67, 68]. The thin tick marks are calculated [57] using the phase-amplitude method [69].

Note that we can only detect events as sequential if the intermediate molecules have appropriate lifetimes. [57, 70]. In other words, the intermediate molecule should have enough time to rotate so that we observe a uniform $N(\theta_{\mathrm{CO,O}})$ distribution. On the other hand, the lifetime of the intermediate molecule can be a maximum of a few nanoseconds. This is due to the limited time window imposed by our imaging technique [70]. Similar to the sequential

channel involving a CO^{2+} intermediate in OCS, the $X^3\Pi$ (ν=2,5,8,9,J=1) and $b^1\Pi$ (ν=3-6) states of CO^{2+} match the peak of KER_{CO}. The other states shown in Fig. 3.9 do not play a role in sequential breakup because they do not have appropriate lifetimes.

3.5 Summary

Strong-field fragmentation of CO_2 into C^++O^++O^+ following triple ionization is studied as an example of three-body breakup involving two identical fragments. We use the native frames method to separate the concerted fragmentation events from the sequential breakup events. It is shown that it is possible to distinguish the step in which each detected O^+ fragment is formed in the sequential breakup process.

Chapter 4

Summary

In summary, we studied two examples of interactions between the strong field of a laser and molecules. The focus of the first study was on controlling the formation of excited neutral D fragments from D_2 molecules. We implemented a single-prism compressor to manipulate the phase of the laser pulses and controlled the dissociation of D_2 molecules. A chirp dependence in the formation of the D* fragments was observed.

Three-body fragmentation of CO_2 into C^++O^++O^+, which involves two identical O^+ fragments, was studied. The native-frames analysis method was used to separate the concerted fragmentation events from the sequential breakup events. We demonstrated how to identify the pathways traversed by the two O^+ fragments in a sequential breakup of CO_2^{3+}.

In addition to the projects discussed in this thesis, I was also involved in other projects led by my colleagues at JRML, as well as a few studies in collaboration with the group of Marcos Dantus at the Michigan State University (MSU) Department of Chemistry. For example, our group has been studying isomerization of $C_2H_2^q$ molecular-ion beams in acetylene and vinylidene configurations. In collaboration with the MSU group, we studied mechanisms for the formation of H_3^+ from alcohol molecules in strong laser fields, and in particular we discussed the role of H_2 roaming in this process [24, 71].

Bibliography

[1] A. H. Zewail, "Laser femtochemistry", Science **242**, 1645 (1988), http://science.sciencemag.org/content/242/4886/1645.

[2] G. Steinmeyer, "A review of ultrafast optics and optoelectronics", J. Opt. A **5**, 1 (2003), http://stacks.iop.org/1464-4258/5/i=1/a=201.

[3] P. B. Corkum and F. Krausz, "Attosecond science", Nature Physics **3**, 381 (2007), https://www.nature.com/articles/nphys620.

[4] F. Krausz and M. Ivanov, "Attosecond physics", Rev. Mod. Phys. **81**, 163 (2009), https://link.aps.org/doi/10.1103/RevModPhys.81.163.

[5] T. Brabec, ed., *Strong field laser physics* (Springer Series in Optical Sciences, 2009).

[6] Z. Chang, *Fundamentals of attosecond optics* (CRC press, 2011), https://www.crcpress.com/Fundamentals-of-Attosecond-Optics/Chang/p/book/9781420089370.

[7] C. J. Joachain, N. J. Kylstra, and R. M. Potvliege, *Atoms in intense laser fields* (Cambridge University Press, 2012).

[8] C. D. Lin, *Attosecond and strong-field physics: principles and applications* (Cambridge University Press, 2018).

[9] S. Svanberg, "Some applications of ultrashort laser pulses in biology and medicine", Meas. Sci. Technol. **12**, 1777 (2001), http://stacks.iop.org/0957-0233/12/i=11/a=304.

[10] M. E. Fermann, A. Galvanauskas, and G. Sucha, *Ultrafast lasers: technology and applications* (CRC Press, 2002), https://www.

crcpress.com/Ultrafast-Lasers-Technology-and-Applications/Fermann-Galvanauskas-Sucha/p/book/9780824708412.

[11] K. Sugioka and Y. Cheng, *Ultrafast laser processing: from micro- to nanoscale* (CRC press, 2013), https://www.crcpress.com/Ultrafast-Laser-Processing-From-Micro--to-Nanoscale/Sugioka-Cheng/p/book/9789814267335.

[12] D. Strickland and G. Mourou, "Compression of amplified chirped optical pulses", Opt. Commun. **55**, 447 (1985), http://www.sciencedirect.com/science/article/pii/0030401885901518.

[13] B. Lasorne and G. Worth, eds., *Coherent control of molecules* (Collaborative Computational Project on Molecular Quantum Dynamics, 2006).

[14] M. Shapiro and P. Brumer, *Quantum control of molecular processes* (Wiley, 2012).

[15] P. Agostini, F. Fabre, G. Mainfray, G. Petite, and N. K. Rahman, "Free-free transitions following six-photon ionization of xenon atoms", Phys. Rev. Lett. **42**, 1127 (1979), https://link.aps.org/doi/10.1103/PhysRevLett.42.1127.

[16] A. l'Huillier, L. A. Lompre, G. Mainfray, and C. Manus, "Multiply charged ions induced by multiphoton absorption in rare gases at 0.53 μm", Phys. Rev. A **27**, 2503 (1983), https://link.aps.org/doi/10.1103/PhysRevA.27.2503.

[17] A. McPherson, G. Gibson, H. Jara, U. Johann, T. S. Luk, I. A. McIntyre, K. Boyer, and C. K. Rhodes, "Studies of multiphoton production of vacuum-ultraviolet radiation in the rare gases", J. Opt. Soc. Am. B **4**, 595 (1987), http://josab.osa.org/abstract.cfm?URI=josab-4-4-595.

[18] P. H. Bucksbaum, A. Zavriyev, H. G. Muller, and D. W. Schumacher, "Softening of the H_2^+ molecular bond in intense laser fields", Phys. Rev. Lett. **64**, 1883 (1990), https://link.aps.org/doi/10.1103/PhysRevLett.64.1883.

[19] V. Roudnev, B. D. Esry, and I. Ben-Itzhak, "Controlling HD^+ and H_2^+ dissociation with the carrier-envelope phase difference of an intense ultrashort laser pulse", Phys. Rev. Lett. **93**, 163601 (2004), https://link.aps.org/doi/10.1103/PhysRevLett.93.163601.

[20] T. Nubbemeyer, K. Gorling, A. Saenz, U. Eichmann, and W. Sandner, "Strong-field tunneling without ionization", Phys. Rev. Lett. **101**, 233001 (2008), https://link.aps.org/doi/10.1103/PhysRevLett.101.233001.

[21] M. Zohrabi, J. McKenna, B. Gaire, N. G. Johnson, K. D. Carnes, S. De, I. A. Bocharova, M. Magrakvelidze, D. Ray, I. V. Litvinyuk, et al., "Vibrationally resolved structure in O_2^+ dissociation induced by intense ultrashort laser pulses", Phys. Rev. A **83**, 053405 (2011), https://link.aps.org/doi/10.1103/PhysRevA.83.053405.

[22] J. McKenna, S. Zeng, J. J. Hua, A. M. Sayler, M. Zohrabi, N. G. Johnson, B. Gaire, K. D. Carnes, B. D. Esry, and I. Ben-Itzhak, "Frustrated tunneling ionization during laser-induced D_2 fragmentation: Detection of excited metastable D^* atoms", Phys. Rev. A **84**, 043425 (2011), https://link.aps.org/doi/10.1103/PhysRevA.84.043425.

[23] A. von Veltheim, B. Manschwetus, W. Quan, B. Borchers, G. Steinmeyer, H. Rottke, and W. Sandner, "Frustrated tunnel ionization of noble gas dimers with Rydberg-electron shakeoff by electron charge oscillation", Phys. Rev. Lett. **110**, 023001 (2013), https://link.aps.org/doi/10.1103/PhysRevLett.110.023001.

[24] N. Ekanayake, M. Nairat, B. Kaderiya, P. Feizollah, B. Jochim, T. Severt, B. Berry, Kanaka Raju P., K. D. Carnes, S. Pathak, et al., "Mechanisms and time-resolved dynamics for trihydrogen cation (H_3^+) formation from organic molecules in strong laser fields", Sci. Rep. **7**, 4703 (2017), https://www.nature.com/articles/s41598-017-04666-w.

[25] B. Manschwetus, T. Nubbemeyer, K. Gorling, G. Steinmeyer, U. Eichmann, H. Rottke, and W. Sandner, "Strong laser field fragmentation of H_2: Coulomb explosion without

double ionization", Phys. Rev. Lett. **102**, 113002 (2009), https://link.aps.org/doi/10.1103/PhysRevLett.102.113002.

[26] U. Eichmann, T. Nubbemeyer, H. Rottke, and W. Sandner, "Acceleration of neutral atoms in strong short-pulse laser fields", Nature **461**, 1261 (2009), https://www.nature.com/articles/nature08481.

[27] J. McKenna, A. M. Sayler, B. Gaire, N. G. Kling, B. D. Esry, K. D. Carnes, and I. Ben-Itzhak, "Frustrated tunnelling ionization during strong-field fragmentation of D_3^+", New J. Phys. **14**, 103029 (2012), http://iopscience.iop.org/article/10.1088/1367-2630/14/10/103029/meta.

[28] W. Zhang, Z. Yu, X. Gong, J. Wang, P. Lu, H. Li, Q. Song, Q. Ji, K. Lin, J. Ma, et al., "Visualizing and steering dissociative frustrated double ionization of hydrogen molecules", Phys. Rev. Lett. **119**, 253202 (2017), https://link.aps.org/doi/10.1103/PhysRevLett.119.253202.

[29] R. R. Jones, D. W. Schumacher, and P. H. Bucksbaum, "Population trapping in Kr and Xe in intense laser fields", Phys. Rev. A **47**, R49 (1993), https://link.aps.org/doi/10.1103/PhysRevA.47.R49.

[30] E. Wells, I. Ben-Itzhak, and R. R. Jones, "Ionization of atoms by the spatial gradient of the pondermotive potential in a focused laser beam", Phys. Rev. Lett. **93**, 023001 (2004), https://link.aps.org/doi/10.1103/PhysRevLett.93.023001.

[31] P. B. Corkum, "Plasma perspective on strong field multiphoton ionization", Phys. Rev. Lett. **71**, 1994 (1993), https://link.aps.org/doi/10.1103/PhysRevLett.71.1994.

[32] T. Morishita and C. D. Lin, "Photoelectron spectra and high Rydberg states of lithium generated by intense lasers in the over-the-barrier ionization regime", Phys. Rev. A **87**, 063405 (2013), https://link.aps.org/doi/10.1103/PhysRevA.87.063405.

[33] A. S. Landsman, A. N. Pfeiffer, C. Hofmann, M. Smolarski, C. Cirelli, and U. Keller,

"Rydberg state creation by tunnel ionization", New J. Phys. **15**, 013001 (2013), http://stacks.iop.org/1367-2630/15/i=1/a=013001.

[34] S. Akturk, X. Gu, M. Kimmel, and R. Trebino, "Extremely simple single-prism ultrashort-pulse compressor", Opt. Express **14**, 10101 (2006), http://www.opticsexpress.org/abstract.cfm?URI=oe-14-21-10101.

[35] X. Ren, A. M. Summers, Kanaka Raju P., A. Vajdi, V. Makhija, C. W. Fehrenbach, N. G. Kling, K. J. Betsch, Z. Wang, M. F. Kling, et al., "Single-shot carrier-envelope-phase tagging using an $f-2f$ interferometer and a phase meter: a comparison", J. Opt. **19**, 124017 (2017), http://stacks.iop.org/2040-8986/19/i=12/a=124017.

[36] M. Zohrabi, Ph.D. thesis, Kansas State University (2014).

[37] A. Weiner, *Ultrafast optics* (Wiley, 2009), https://www.wiley.com/en-us/Ultrafast+Optics-p-9780471415398.

[38] J.-C. Diels and W. Rudolph, *Ultrashort laser pulse phenomena* (Elsevier, 2006).

[39] R. Szipöcs, K. Ferencz, C. Spielmann, and F. Krausz, "Chirped multilayer coatings for broadband dispersion control in femtosecond lasers", Opt. Lett. **19**, 201 (1994), http://ol.osa.org/abstract.cfm?URI=ol-19-3-201.

[40] E. Treacy, "Optical pulse compression with diffraction gratings", IEEE J. Quantum Electron. **5**, 454 (1969), https://ieeexplore.ieee.org/document/1076303/authors#authors.

[41] R. L. Fork, O. E. Martinez, and J. P. Gordon, "Negative dispersion using pairs of prisms", Opt. Lett. **9**, 150 (1984), http://ol.osa.org/abstract.cfm?URI=ol-9-5-150.

[42] K. W. DeLong, R. Trebino, and D. J. Kane, "Comparison of ultrashort-pulse frequency-resolved-optical-gating traces for three common beam geometries", J. Opt. Soc. Am. B **11**, 1595 (1994), http://josab.osa.org/abstract.cfm?URI=josab-11-9-1595.

[43] R. L. Fork, O. E. Martinez, and J. P. Gordon, "Negative dispersion using pairs of prisms", Opt. Lett. **9**, 150 (1984), http://ol.osa.org/abstract.cfm?URI=ol-9-5-150.

[44] B. Berry, M. Zohrabi, D. Hayes, U. Ablikim, B. Jochim, T. Severt, K. D. Carnes, and I. Ben-Itzhak, "Note: Determining the detection efficiency of excited neutral atoms by a microchannel plate detector", Rev. Sci. Instrum. **86**, 046103 (2015), https://aip.scitation.org/doi/full/10.1063/1.4916953.

[45] J. L. Wiza, "Microchannel plate detectors", J. Nucl. Instrum. Methods **162**, 587 (1979), https://www.sciencedirect.com/science/article/abs/pii/0029554X79907341.

[46] A. Palacios, J. L. Sanz-Vicario, and F. Martín, "Theoretical methods for attosecond electron and nuclear dynamics: applications to the H_2 molecule", J. Phys. B **48**, 242001 (2015), http://stacks.iop.org/0953-4075/48/i=24/a=242001.

[47] T. E. Sharp, "Potential-energy curves for molecular hydrogen and its ions", At. Data Nucl. Data Tables **2**, 119 (1970), https://www.sciencedirect.com/science/article/pii/S0092640X70800079.

[48] B. Whitaker, ed., *Imaging in Molecular Dynamics—Technology and applications,* (Cambridge University Press, New York, 2003).

[49] J. Ullrich, ed., *Ten Years of COLTRIMS and Reaction Microscopes* (Max-Planck-Institut fur Kernpysik Heidelberg, Heidelberg, Germany, 2004).

[50] U. Werner, K. Beckord, J. Becker, and H. O. Lutz, "3D imaging of the collision-induced Coulomb fragmentation of water molecules", Phys. Rev. Lett. **74**, 1962 (1995), https://link.aps.org/doi/10.1103/PhysRevLett.74.1962.

[51] N. Neumann, D. Hant, L. P. H. Schmidt, J. Titze, T. Jahnke, A. Czasch, M. S. Schöffler, K. Kreidi, O. Jagutzki, H. Schmidt-Böcking, et al., "Fragmentation dynamics of CO_2^{3+} investigated by multiple electron capture in collisions with slow highly

charged ions", Phys. Rev. Lett. **104**, 103201 (2010), https://link.aps.org/doi/10.1103/PhysRevLett.104.103201.

[52] A. Hishikawa, H. Hasegawa, and K. Yamanouchi, "Sequential three-body coulomb explosion of CS_2 in intense laser fields appearing in momentum correlation map", Chem. Phys. Lett. **361**, 245 (2002), http://www.sciencedirect.com/science/article/pii/S0009261402008801.

[53] C. Wu, C. Wu, D. Song, H. Su, Y. Yang, Z. Wu, X. Liu, H. Liu, M. Li, Y. Deng, et al., "Nonsequential and sequential fragmentation of ${CO_2}^{3+}$ in intense laser fields", Phys. Rev. Lett. **110**, 103601 (2013), https://link.aps.org/doi/10.1103/PhysRevLett.110.103601.

[54] A. Ramadhan, B. Wales, R. Karimi, I. Gauthier, M. MacDonald, L. Zuin, and J. Sanderson, "Ultrafast molecular dynamics of dissociative ionization in OCS probed by soft X-ray synchrotron radiation", Journal of Physics B: Atomic, Molecular and Optical Physics **49**, 215602 (2016), http://stacks.iop.org/0953-4075/49/i=21/a=215602.

[55] Z. Shen, E. Wang, M. Gong, X. Shan, and X. Chen, "Fragmentation dynamics of carbonyl sulfide in collision with 500 eV electron", The Journal of Chemical Physics **145**, 234303 (2016), https://doi.org/10.1063/1.4972064.

[56] S. Hsieh and J. H. D. Eland, "Reaction dynamics of three-body dissociations in triatomic molecules from single-photon double ionization studied by a time- and position-sensitive coincidence method", J. Phys. B **30**, 4515 (1997), http://stacks.iop.org/0953-4075/30/i=20/a=015.

[57] J. Rajput, T. Severt, B. Berry, B. Jochim, P. Feizollah, B. Kaderiya, M. Zohrabi, U. Ablikim, F. Ziaee, Kanaka Raju P., et al., "Native frames: Disentangling sequential from concerted three-body fragmentation", Phys. Rev. Lett. **120**, 103001 (2018), https://link.aps.org/doi/10.1103/PhysRevLett.120.103001.

[58] T. Severt, J. Rajput, B. Berry, B. Jochim, P. Feizollah, B. Kaderiya, M. Zohrabi, U. Ablikim, F. Zaiee, Kanaka Raju P., et al., "Native frames: A new approach for separating sequential and concerted three-body fragmentation", Phys. Rev. A (2018), in preparation.

[59] J. Ullrich, R. Moshammer, R. Dörner, O. Jagutzki, V. Mergel, H. Schmidt-Böcking, and L. Spielberger, "Recoil-ion momentum spectroscopy", J. Phys. B **30**, 2917 (1997), http://stacks.iop.org/0953-4075/30/i=13/a=006.

[60] R. Dörner, V. Mergel, O. Jagutzki, L. Spielberger, J. Ullrich, R. Moshammer, and H. Schmidt-Böcking, "Cold target recoil ion momentum spectroscopy: a 'momentum microscope' to view atomic collision dynamics", Phys. Rep. **330**, 95 (2000), http://www.sciencedirect.com/science/article/pii/S037015739900109X.

[61] J. Ullrich, R. Moshammer, A. Dorn, R. Dörner, L. P. H. Schmidt, and H. Schmidt-Böcking, "Recoil-ion and electron momentum spectroscopy: reaction-microscopes", Rep. Prog. Phys. **66**, 1463 (2003), http://stacks.iop.org/0034-4885/66/i=9/a=203.

[62] A. Rudenko, V. Makhija, A. Vajdi, T. Ergler, M. Schürholz, R. K. Kushawaha, J. Ullrich, R. Moshammer, and V. Kumarappan, "Strong-field-induced wave packet dynamics in carbon dioxide molecule", Faraday Discuss. **194** (2016), https://pubs.rsc.org/ru/content/articlelanding/2016/fd/c6fd00152a/unauth#!divAbstract.

[63] R. Trebino, K. W. DeLong, D. N. Fittinghoff, J. N. Sweetser, M. A. Krumbügel, B. A. Richman, and D. J. Kane, "Measuring ultrashort laser pulses in the time-frequency domain using frequency-resolved optical gating", Rev. Sci. Instrum. **68**, 3277 (1997), https://doi.org/10.1063/1.1148286.

[64] V. L. B. de Jesus, B. Feuerstein, K. Zrost, D. Fischer, A. Rudenko, F. Afaneh, C. D. Schröter, R. Moshammer, and J. Ullrich, "Atomic structure dependence of nonsequential double ionization of He, Ne and Ar in strong laser pulses", J. Phys. B **37**, L161 (2004), http://stacks.iop.org/0953-4075/37/i=8/a=L03.

[65] C. D. Lin, "Hyperspherical coordinate approach to atomic and other coulombic three-body systems", Phys. Rep. **257**, 1 (1995), http://www.sciencedirect.com/science/article/pii/037015739400094J.

[66] T. Šedivcová-Uhlíková, P. R. Kaprálová-Ždánská, and V. Špirko, "Radiative transition probabilities of CO^{2+}", Int. J. Quantum Chem. **107**, 2654 (2007), https://onlinelibrary.wiley.com/doi/abs/10.1002/qua.21448.

[67] M. Lundqvist, P. Baltzer, D. Edvardsson, L. Karlsson, and B. Wannberg, "Novel time of flight instrument for doppler free kinetic energy release spectroscopy", Phys. Rev. Lett. **75**, 1058 (1995), https://link.aps.org/doi/10.1103/PhysRevLett.75.1058.

[68] M. Hochlaf, R. I. Hall, F. Penent, H. Kjeldsen, P. Lablanquie, M. Lavollée, and J. H. D. Eland, "Threshold photoelectrons coincidence spectroscopy of N_2^{2+} and CO^{2+} ions", Chem. Phys. **207**, 159 (1996), https://www.sciencedirect.com/science/article/abs/pii/0301010496000560.

[69] E. Y. Sidky and I. Ben-Itzhak, "Phase-amplitude method for calculating resonance energies and widths for one-dimensional potentials", Phys. Rev. A **60**, 3586 (1999), https://link.aps.org/doi/10.1103/PhysRevA.60.3586.

[70] B. Jochim, R. Erdwien, Y. Malakar, T. Severt, B. Berry, P. Feizollah, J. Rajput, B. Kaderiya, W. L. Pearson, K. D. Carnes, et al., "Three-dimensional momentum imaging of dissociation in flight of metastable molecules", New J. Phys. **19**, 103006 (2017), http://stacks.iop.org/1367-2630/19/i=10/a=103006.

[71] N. Ekanayake, T. Severt, M. Nairat, N. P. Weingartz, B. M. Farris, B. Kaderiya, P. Feizollah, B. Jochim, F. Ziaee, K. Borne, et al., "H_2 roaming chemistry and the formation of H_3^+ from alcohols in strong laser fields", Nat. Commun. (2018), accepted.